Pergamon

Int. J. Multiphase Flow Vol. 20, No. 2, pp. 235–247, 1994

0301-9322/94 $7.00 + 0.00

FLOODING IN VERTICAL TUBES—II

A FILM MODEL FOR ENTRY REGION FLOODING

C. E. Lacy and A. E. Dukler✠
Chemical Engineering Department, University of Houston, Houston, TX 77204, U.S.A.

(Received 20 April 1993; in revised form 16 September 1993)

Abstract—A new flooding mechanism is explored for porous tube feed systems based on the concept that flow reversal takes place inside the liquid film at the feed location. The model is developed, assuming that the flow field in the liquid film at any axial position can be represented by the time-average film thickness existing there. Thus, it makes the radical assumption that the interfacial waves exert their influence only by modifying the shear stress in the gas flowing over the film. A 2-D numerical simulation was constructed which solved for both the flow field inside the film and the shape of the free interface. The numerical results show that this film mechanism is a viable approach for modeling flooding, as reasonable values of the interfacial shear stress from the upward gas flow can reproduce the experimentally measured film thickness. This work also suggests that the pressure gradient developed inside the entry is only partially due to interfacial shear. Gas-phase accelerations, due to the wave motion, contribute the remainder of the measured pressure gradient.

Key Words: flooding, entry region, film flow

INTRODUCTION

Flooding in falling-film systems has been the subject of numerous theoretical and experimental studies for over 50 years. During this time, a large number of empirical correlations as well as mechanistically-based models have been formulated to predict the onset of flooding, where liquid first begins to flow upward. These have been reviewed recently by Bankoff & Lee (1986). When these approaches are compared to data, however, none of them are able to predict flooding over a significant range of flow conditions, fluid properties, tube size, length or entry configurations. This is because the mechanisms on which these models are based are still poorly understood. In part I (Lacy & Dukler 1994, this issue, pp. 219–233) new data were presented for a flow loop in which the feed was introduced through a porous tube located partway up the column. These data were used to evaluate previously suggested mechanisms. In particular, no evidence was found to support mechanisms based on waves causing flooding. That is, the growth of waves sufficient to block the tube or the propagation of waves along the film in the upward direction past the feed location did not take place. Instead, the data suggest that, at flooding, a change occurs within the film formed at the liquid entry, such that the liquid flows upward in the film at the top of the feed zone and down at the bottom. To test this possiblity, this paper presents a film model which describes how the liquid can split between the upflow and downflow at the feed location. It will be shown that the model gives a realistic mechanism for flooding and is limited, at present, only by the ability to estimate the interfacial shear stress applied to the film by the gas flow. The concept that flooding takes place at the feed location was suggested by Zabaras & Dukler (1988), who showed that the behaviors above and below the feed were uncoupled for sinter feed systems. This conclusion was confirmed in experiments by Govan *et al.* (1991).

NUMERICAL TECHNIQUE

Overview

In the film model to be tested, the steady-state flow equations will be solved numerically for laminar film flow across the entry region, where liquid is injected through the wall. In this approach,

---

✠Deceased February 1994.

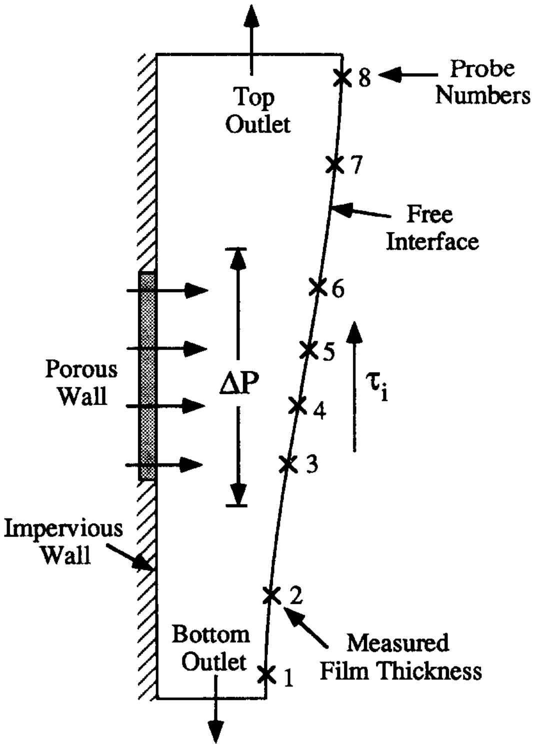

Figure 1. Sketch of the feed region.

the rather radical assumption is made that the flow field of the liquid film, for each axial location in the feed zone, can be represented by the time-average of the film thickness. The waves that always exist on the liquid film are assumed to make their influence felt only by modifying certain flow characteristics of the gas phase, such as the shear stress at the interface and accelerations. Perhaps surprisingly, it will be shown that such an extreme premise leads to acceptable agreement between the model and the experiment. The modeling task is complicated by the fact that the actual shape of the free interface is unknown and must be computed as part of the overall solution.

Figure 1 shows a sketch of the liquid feed region used in the numerical simulations. The liquid enters the tube, joins the film through the center third of the wall and leaves through the top and bottom planes. The feed rate through the porous wall is specified. At the free interface the upward gas flow produces an interfacial shear stress, τ_i, acting on the film. The mean film thickness is known at 8 positions along the interface, as shown in figure I-7 (part I—figure 7). Each of these are represented by an × in figure 1. In addition, the average pressure gradient across the injection region has been measured. Given the feed rate, fluid properties and measured pressure drop, the objective is to compute the shape and location of the interface and the split of the liquid between the upflow and downflow for a specified interfacial shear stress distribution. The condition for which the upflow first becomes nonzero is the flooding condition. The problem is compounded by the need to search for the location of a free interface. Furthermore, the interfacial shear cannot be calculated directly from the pressure gradient in the presence of a wavy surface, since part of this pressure drop is attributable to form drag. For this reason, and for computational convenience, the approach to the problem is inverted. In this study the split between the upflow and downflow is specified to match the experimental data at flooding ($<10\%$ upflow). Then a shear stress profile is assumed, from which the shape of the domain and the flow field are computed by iteration until the normal pressure condition is satisfied at all interfacial locations in the feed zone. This process is repeated for various stress profiles until a film thickness profile is computed which is in optimal agreement with the measured one. The resulting stress profile is then examined for its physical reality.

Solving the hydrodynamic problem in the domain shown in figure 1 would involve discretizing the Navier–Stokes equations on a 2-D domain where the free interface changes during the

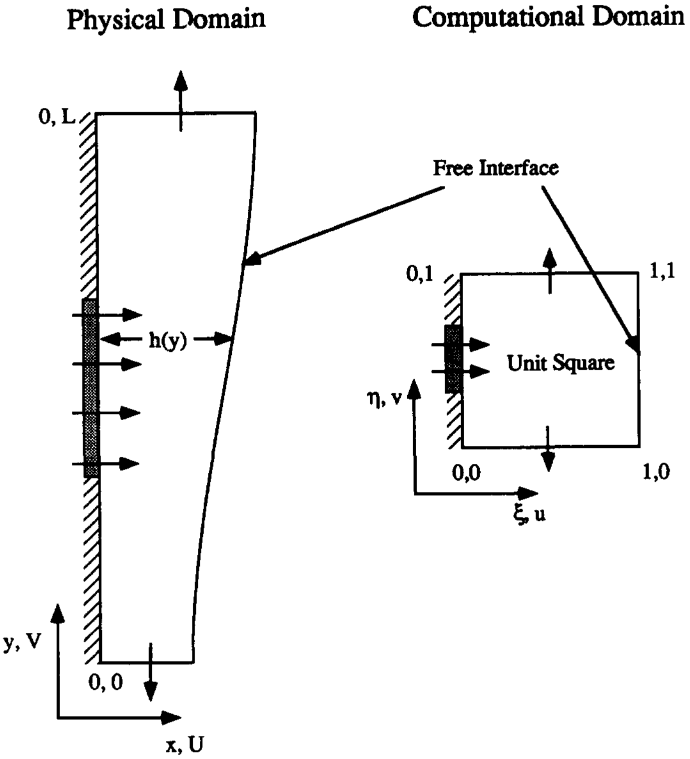

Figure 2. Mapping of the physical problem onto a square grid.

simulation. This change in the domain shape also alters the position of the numerical grid points on which the hydrodynamic problem must be solved. A nonchanging grid for discretizing the flow equations is preferred. A method to accomplish this task is to orthogonally map the physical domain (x, y) onto a unit square (ξ, η), as shown in figure 2. In this case the equations are discretized on a nonchanging square grid instead of the of the (x, y) domain. To implement this approach, the governing equations must be formulated in the (ξ, η) domain, and a method must be chosen for the mapping.

Navier–Stokes Equations

To develop the required form of the Navier–Stokes equations, first consider the relationships between the orthogonal coordinate systems (x, y) and (ξ, η). The differential length, ds, is given by

$$\mathrm{d}s^2 = \mathrm{d}x^2 + \mathrm{d}y^2 = h_\xi^2\,\mathrm{d}\xi^2 + h_\eta^2\,\mathrm{d}\eta^2, \qquad [1]$$

where h_ξ and h_η are the "scale factors" relating the difference in length scales between the two domains. They are defined as

$$h_\xi = \sqrt{\left(\frac{\partial x}{\partial \xi}\right)^2 + \left(\frac{\partial y}{\partial \xi}\right)^2} \quad \text{and} \quad h_\eta = \sqrt{\left(\frac{\partial x}{\partial \eta}\right)^2 + \left(\frac{\partial y}{\partial \eta}\right)^2}. \qquad [2]$$

The continuity equation and the Navier–Stokes equations can now be expressed in terms of these scale factors for 2-D steady laminar flow. Since the average film thickness is only a few percent of the tube radius, the flow field will be considered planar instead of axisymmetric. The continuity equation can now be defined as

$$\nabla \cdot (\rho \mathbf{V}) = \frac{1}{h_\xi h_\eta}\left[\frac{\partial}{\partial \xi}(h_\eta \rho u) + \frac{\partial}{\partial \eta}(h_\xi \rho v)\right] = 0, \qquad [3]$$

where ρ is the fluid density, **V** is the velocity vector and u and v are the velocities in the ξ and η directions, respectively. The equation for steady-state flow is given by

$$\nabla \cdot (\rho \mathbf{V}\mathbf{V} + P\mathbf{I} - \tau) = \mathbf{B}, \qquad [4]$$

where P is the pressure, $\mathbf{I}$ is the unit tensor, τ is the viscous shear stress and $\mathbf{B}$ is the body force. The resulting equations in terms of the rate of strain, ϵ_{ij}, can be expressed as

$$\frac{\partial}{\partial \xi}(h_\eta \rho u^2) + \frac{\partial}{\partial \eta}(h_\xi \rho uv) + \rho uv \frac{\partial h_\xi}{\partial \eta} - \rho v^2 \frac{\partial h_\eta}{\partial \xi} = h_\xi h_\eta B_\xi$$
$$- h_\eta \frac{\partial P}{\partial \xi} + \frac{\partial}{\partial \xi}(2\mu h_\eta \epsilon_{\xi\xi}) + \frac{\partial}{\partial \eta}(2\mu h_\xi \epsilon_{\xi\eta}) + 2\mu\left(\epsilon_{\xi\eta}\frac{\partial h_\xi}{\partial \eta} - \epsilon_{\eta\eta}\frac{\partial h_\eta}{\partial \xi}\right) \quad [5]$$

and

$$\frac{\partial}{\partial \xi}(h_\eta \rho uv) + \frac{\partial}{\partial \eta}(h_\xi \rho v^2) + puv \frac{\partial h_\eta}{\partial \xi} - \rho u^2 \frac{\partial h_\xi}{\partial \eta} = h_\xi h_\eta B_\eta$$
$$- h_\xi \frac{\partial P}{\partial \eta} + \frac{\partial}{\partial \xi}(2\mu h_\eta \epsilon_{\xi\eta}) + \frac{\partial}{\partial \eta}(2\mu h_\xi \epsilon_{\eta\eta}) + 2\mu\left(\epsilon_{\xi\eta}\frac{\partial h_\eta}{\partial \xi} - \epsilon_{\xi\xi}\frac{\partial h_\xi}{\partial \eta}\right) \quad [6]$$

for the ξ and η directions, respectively, where μ is the fluid viscosity. The components of the rate-of-strain tensor and the complete Navier–Stokes equations in terms of u and v are given in the appendix. The boundary conditions at the wall, $\xi = 0$, are

$$u(0, \eta) = \text{known} \quad \text{and} \quad v(0, \eta) = 0, \quad [7]$$

which corresponds to the velocity normal to the porous and impervious walls being specified and to the no-slip boundary condition. At the top and bottom of the domain, $\eta = 0$ or 1, the boundary conditions are given by

$$u(\xi, 0) = u(\xi, 1) = 0 \quad \text{and} \quad \frac{\partial v(\xi, 0)}{\partial \eta} = \frac{\partial v(\xi, 1)}{\partial \eta} = 0, \quad [8]$$

which assumes that the flow field approaches 1-D nonaccelerating flow having a constant film thickness at the top and bottom of the domain. For the free interface, $\xi = 1$, the tangential and normal stresses can be expressed by

$$\tau_i = \frac{\mu}{h_\xi}\left(\frac{\partial v}{\partial \xi} - \frac{v}{h_\eta}\frac{\partial h_\eta}{\partial \xi}\right) \quad [9]$$

and

$$P_L - 2\mu\epsilon_{\xi\xi} = P_G + \frac{\sigma}{h_\xi h_\eta}\frac{\partial h_\eta}{\partial \xi}, \quad [10]$$

where σ is the surface tension and the subscripts L and G refer to the liquid and gas side of the interface, respectively.

The flow field is computed by solving [5] and [6] on the unit square. For this purpose a computer code was constructed based on the Teach-T code of Gosman & Ideriah (1976). This is a control-volume formulation on a staggered-grid system which uses the SIMPLIER pressure/continuity procedure as described by Patankar (1980). To properly handle the convective terms in [5] and [6], Huang *et al.* (1985) studied different discretization schemes as better alternatives to the widely used upwind differencing scheme and found the QUICK scheme of Leonard (1979) to be the most satisfactory. To overcome stability problems inherent in the original QUICK formulation, this study incorporates an improved version developed by Pollard & Siu (1982) known as QUICKER (extended and revised).

Mapping Technique

The "strong constraint" method developed by Ryskin & Leal (1983) was used to compute the scale factors for the mapping and to converge on the correct interfacial shape. In this method two Laplace equations, given by

$$\frac{\partial}{\partial \xi}\left(f\frac{\partial x}{\partial \xi}\right) + \frac{\partial}{\partial \eta}\left(\frac{1}{f}\frac{\partial x}{\partial \eta}\right) = 0 \quad [11]$$

and

$$\frac{\partial}{\partial \xi}\left(f\frac{\partial y}{\partial \xi}\right)+\frac{\partial}{\partial \eta}\left(\frac{1}{f}\frac{\partial y}{\partial \eta}\right)=0, \qquad [12]$$

must be solved for the x and y directions. The function $f(\xi, \eta)$, known descriptively as the distortion function, controls the positioning of the grid points in the (x, y) plane and is defined simply as

$$f(\xi, \eta) \equiv \frac{h_\eta}{h_\xi}. \qquad [13]$$

One starts with a simple shape in the physical domain that is geometrically similar to what the actual shape of the domain should be, so that the initial values for the scale factors, and therefore f, are known. For the entry region, a rectangle was chosen as the initial shape. The initial value of f was thus the ratio of the adjacent side-lengths, which corresponds to a rectangular grid in the (x, y) plane.

To obtain the mapping, [11] and [12] were each solved on separate unit squares as shown in figure 3. The boundary conditions must satisfy orthogonality constraints, which were given by Ryskin & Leal (1983) as

$$f\frac{\partial x}{\partial \xi}=\frac{\partial y}{\partial \eta} \quad \text{and} \quad \frac{\partial x}{\partial \eta}=-f\frac{\partial y}{\partial \xi}. \qquad [14]$$

For three of the four sides, either $x(\xi, \eta)$ or $y(\xi, \eta)$ is a constant. As its derivative along that same side is therefore zero, [14] shows that the derivative of the other $x(\xi, \eta)$ or $y(\xi, \eta)$ variable in the direciton normal to that side is also zero, hence the boundary conditions shown in figure 3. This is not the case, however, for the free interface located at $\xi = 1$. In fact, it is through the specifying of this boundary condition at $\xi = 1$ that the free interface is actually changed during the solution process. As this change cannot be done *a priori* and still maintain an orthogonal grid, Ryskin & Leal (1983) proposed that the scale factor $h_\xi(\xi, \eta)$ at $\xi = 1$ be changed. The reasoning behind this approach is the following. As the normal to the free surface is also the normal to the $\xi = 1$ boundary, a point on this boundary at $\eta = \eta_i$, for example, can be moved inward or outward along the ξ coordinate by simply decreasing or increasing $h_\xi(1, \eta)$ for each $\eta = \eta_i$ along the interface ($\xi = 1$). When the values of $h_\xi(1, \eta_i)$ are thus changed, new values of $x(\xi, \eta)$, $y(\xi, \eta)$ and the scale factors can be determined throughout the domain.

For the initial rectangular geometry, the scale factors are equal at all locations in the domain. At the end of $n - 1$ iterations in order to update the domain shape, the value of $h_\xi(1, \eta)$ for any $\eta = \eta_i$ is set equal to its value at the $(n - 1)$th iteration plus a small change, $\delta^{n-1}(\eta_i)$. This gives

$$h_\xi^n(1, \eta_i) = h_\xi^{n-1}(1, \eta_i) + \delta^{n-1}(\eta_i), \qquad [15]$$

where $\delta^{n-1}(\eta_i)$ is computed using the imbalance in the normal pressure at the interface evaluated from the last solution of the equations of motion. The method developed for computing $\delta^{n-1}(\eta_i)$ appears in the appendix as [A15].

The solution procedure for solving both the hydrodynamic problem and converging on the interfacial shape is as follows:

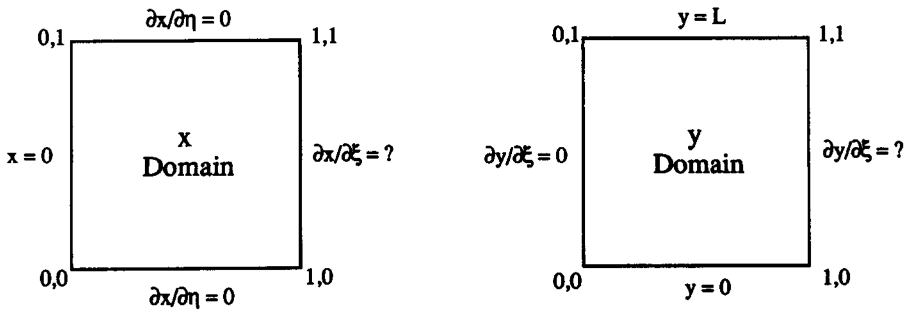

Figure 3. Boundary conditions to compute the mapping.

(1) Select the initial rectangular shape and number of grid points, thus specifying f and $h_\xi(1, \eta)$.
(2) Solve [5] and [6] subject to the boundary conditions [7]–[9].
(3) Calculate the normal pressure imbalance using [10].
(4) Calculate δ from [A15].
(5) Update the value of $h_\xi(1, \eta)$ in [15].
(6) Solve [11] and [12] using the updated value of $h_\xi(1, \eta)$ to obtain a new mapping and the new shape of the domain in the (x, y) plane.
(7) Repeat steps 2–5 until convergence.

To decrease the required computing time, the equations in steps 2 and 6 are solved using a weak convergence criteria for each iteration, since an accurate solution is not necessary at the intermediate steps. For a 30 × 30 grid for u, v and P, the numerical simulation requires 5–30 min on a CRAY-YMP. This includes the computer time needed to carry out the mapping on a 59 × 59 grid.

Interfacial Shear Stress and Pressure Gradient Profiles

To complete the specification of the problem, the axial profile of the interfacial shear stress and the pressure gradient must be approximated across the feed zone. These values are estimated at the top and bottom outlets (see figure 1) by assuming that the liquid is in parallel flow, as indicated by the near-constant values of the mean film thickness at those two locations. The 1-D Navier–Stokes equation for an incompressible fluid is given by

$$0 = -\frac{\mathrm{d}P}{\mathrm{d}y} - \rho g + \mu \frac{\partial^2 V}{\partial x^2}, \qquad [16]$$

with boundary conditions

at $x = 0$ $$V = 0 \qquad [17a]$$

and

at $x = h$ $$\frac{\partial V}{\partial x} = \frac{\tau_i}{\mu}, \qquad [17b]$$

where g is the gravitational acceleration. Solving [16] for V and integrating the resulting velocity profile over the film thickness, h, yields

$$\frac{\mathrm{d}P}{\mathrm{d}y} = -\rho g + \frac{3\tau_i}{2h} + \frac{3\mu\Gamma_d}{h^3}, \qquad [18]$$

where Γ_d is the volumetric rate at which liquid flows downward per unit perimeter. Given the values of h and Γ_d from the experimental data, τ_i can be determined from a force balance over the gas core. For gas flow in the absence of accelerations, as would exist for flow over a smooth film, this balance yields

$$\tau_i = -\frac{(D - 2h)}{4} \frac{\mathrm{d}P}{\mathrm{d}y}, \qquad [19]$$

where D is the pipe diameter. As the pressure gradient is the same in both phases for 1-D flow, [18] and [19] can be combined to give

$$\tau_i = 2\left(\frac{D - 2h}{3D + 2h}\right)\left(\rho g h - \frac{3\mu\Gamma_d}{h^2}\right), \qquad [20]$$

for locations below the feed, and

$$\tau_i = 2\left(\frac{D - 2h}{3D + 2h}\right)\left(\rho g h + \frac{3\mu\Gamma_u}{h^2}\right), \qquad [21]$$

for locations above the feed; where Γ_u is the volumetric rate of liquid flowing upward per unit perimeter. For a given split of the injected liquid between the upflow and downflow, Γ_d and Γ_u are known along with the film thickness. Thus, τ_i can be calculated at the bottom and top outlets from [20] and [21], with the pressure gradients determined from [19].

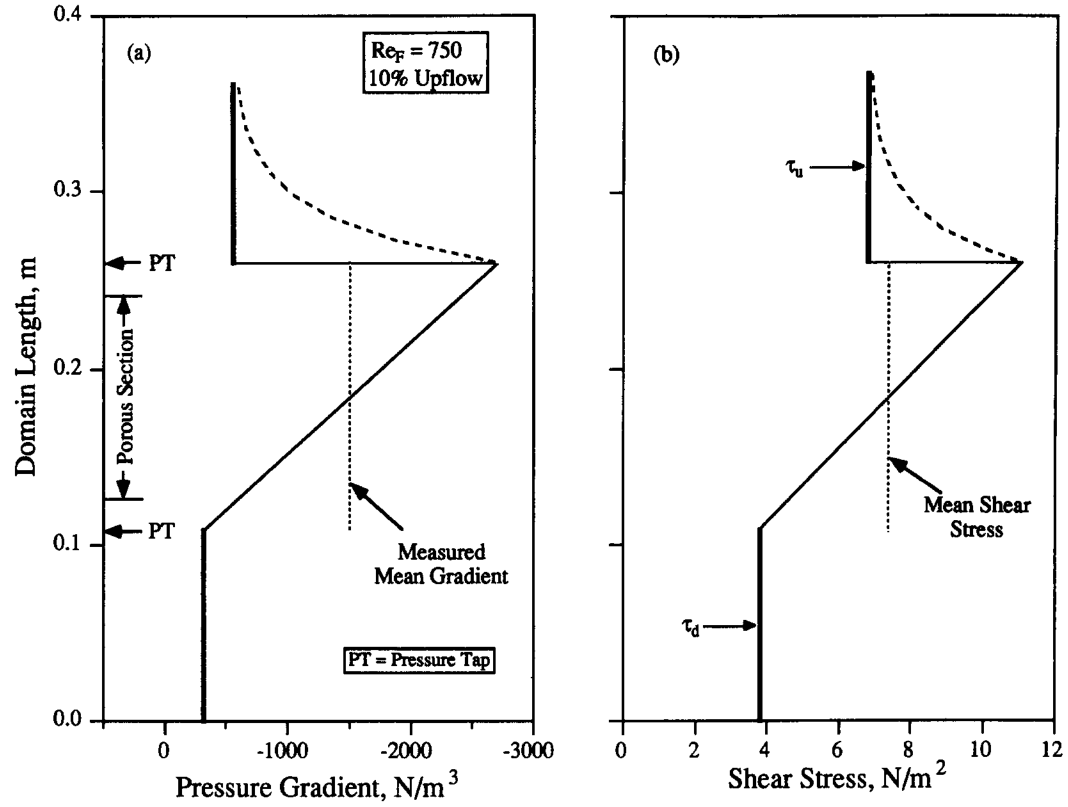

Figure 4. Profiles for the interfacial shear stress and the pressure gradient.

Measurements of the pressure gradients below the porous feed section between probes 1 and 3 (see figure 1) are in approximate agreement with the gradients computed from [19] and [20]. Since these equations were developed for a wave-free interface, one would expect the wave action to be suppressed at the bottom outlet. This is in agreement with the measured wave trace from probe 1 in figure I-6, which shows that highly-damped wave motion exists there. However, the pressure gradient (and presumably the interfacial shear) measured across the feed is much higher than is measured either above or below the feed. Based on these observations, and in the absence of additional information, a linear pressure gradient and shear stress distributions across the porous section are assumed, as shown in figure 4. For the pressure gradient, the measured mean value specifies the slope. Past the maximum the local gradient probably decays gradually as indicated by the dashed line. For computational ease the step change is used. Numerical computations show a negligible difference in the computed film thickness profile from the two pressure gradient profiles.

Shear stress profiles were established by selecting a mean stress and allowing it to vary linearly, as shown in figure 4(b). Then, the average shear stress, τ_{av}, between the two pressure tap locations can be compared with the stress calculated from the measured pressure gradient across the same axial length, τ^*, assuming no accelerations in the gas phase. In addition to interfacial shear, the pressure gradient results from these gas-phase accelerations due to flow around the large interfacial waves and to acceleration of the entrained drops (Lopes & Dukler 1986). Thus, τ_{av}/τ^* would be expected to be < 1.0.

SIMULATION RESULTS

Numerical simulations of the entry region were performed for three liquid feed rates corresponding to flooding data collected in part I for a 50.8 mm i.d. vertical tube. For each feed rate, the split of the liquid between the upflow and downflow was measured in addition to the film thickness and the pressure gradient across the feed. These data corresponded to the lowest gas rate in which a well-developed cocurrent gas–liquid flow existed above the liquid entry region. Table 1 lists these

Table 1

Liquid feed rate, Re_F	Liquid upflow (%)	Gas rate, Re_G
300	6	42,500
750	10	37,600
1500	1	33,300

flow conditions in terms of the Reynolds number, $Re_F = 4\Gamma/\mu$, where Γ is the volumetric liquid flowrate per unit perimeter. Though data were collected at even higher liquid rates in part I, these were not simulated because of the possibility of turbulent flow.

In figure 5, the computed interfacial shapes for each of the cases are compared to the experimental film thickness values. Computations were carried out for a series of interfacial shear ratios, τ_{av}/τ^*. Small sudden changes in the slope of the computed profiles can be observed at the axial position near the top of the porous section. Whether this is a computational artifact due to the discontinuity there or whether it is physically real is not yet known. Solutions with a finer grid show similar results. A value of this shear stress ratio of 0.4, in general, gives agreement well within the ± 0.05 mm error bound for the measured thicknesses. The result meets the criteria of τ_{av}/τ^* being < 1.0. Furthermore, the very large wave structure measured in the feed zone implies the existence of large accelerations due to flow over these waves.

This study involves an analysis of the flow field in the liquid film. Before the model can be fully predictive for flooding, a study of accelerations in the gas phase flowing over a wavy surface will be needed. Then, it will be possible to compute τ_{av}/τ^*. However, even before this is done, it seems possible to arrive at a qualitative judgment that the feed-splitting mechanism proposed here for flooding is reasonable.

The nature of the flow field in the liquid film can be discerned from the streamline map in figure 6 and the velocity profiles shown in figure 7, both for $Re_F = 750$. Splitting of the flow in the film seems to occur with most of the liquid entering the porous section flowing downward and then the reversal of the flow first takes place near the interface as a result of the interfacial shear.

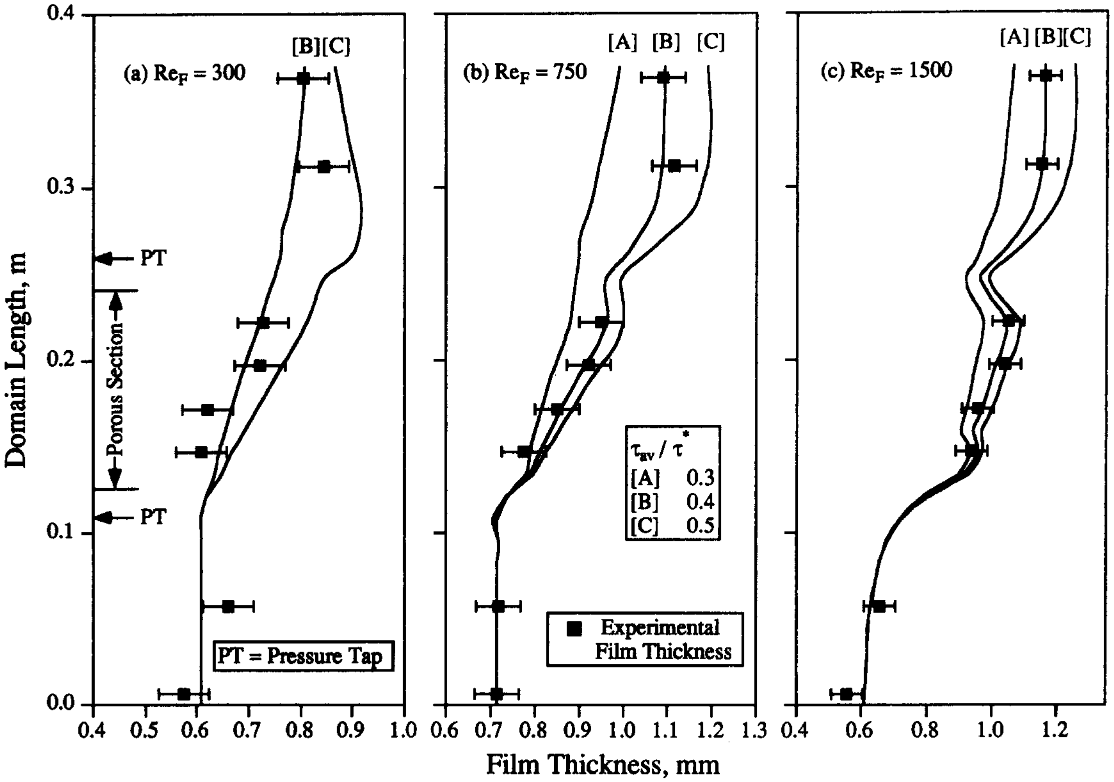

Figure 5. Numerical results for each liquid rate at flooding.

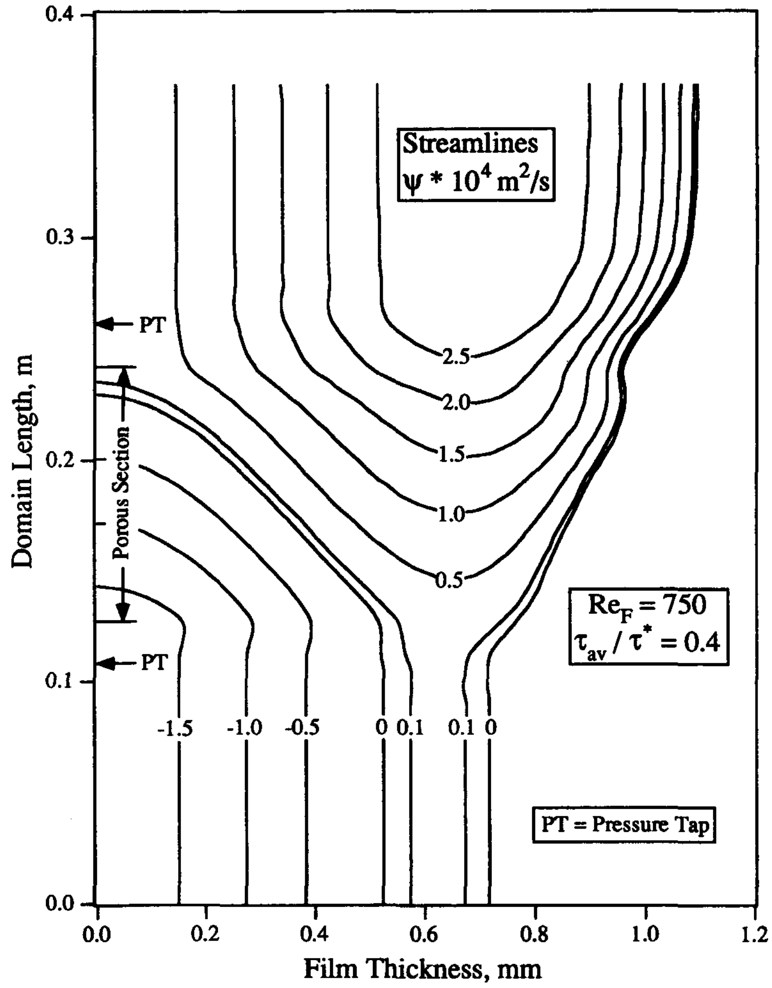

Figure 6. Streamline map for $Re_F = 750$.

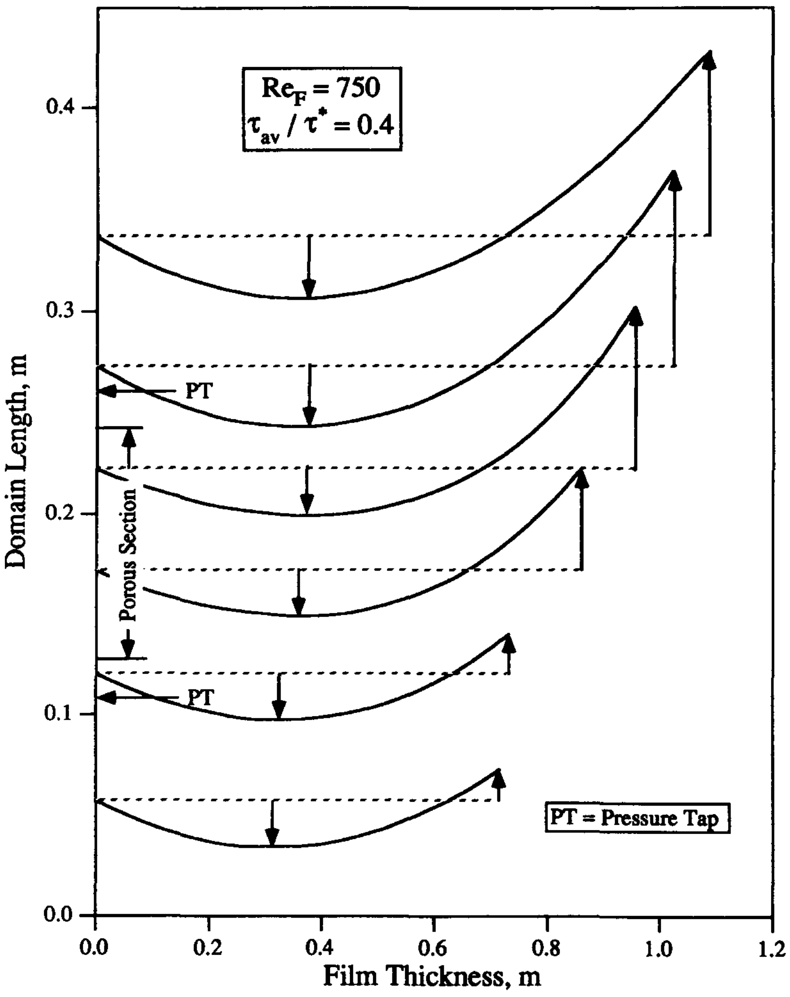

Figure 7. Velocity profiles for $Re_F = 750$.

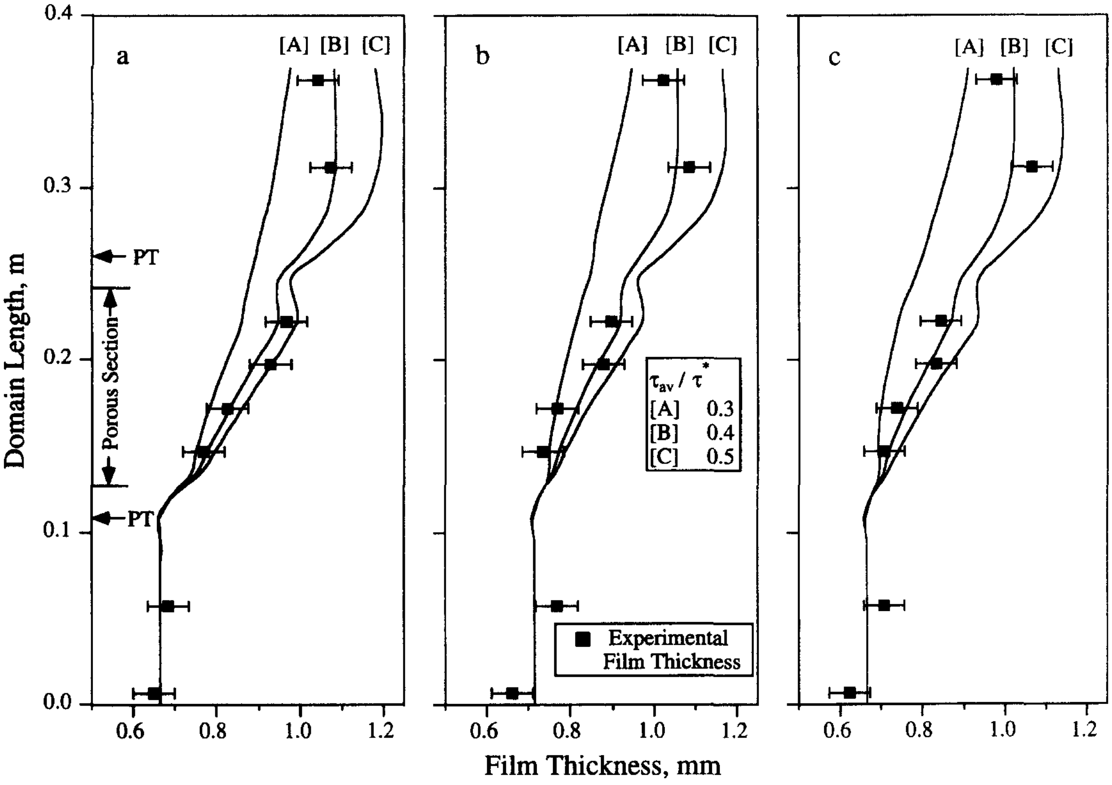

Figure 8. Effect of increasing the liquid upflow rate, $Re_F = 750$. Upflow: (a) 21%; (b) 55%; (c) 75%.

Figure 8 shows the effect of increasing the upflow rate past the flooding point for $Re_F = 750$. For each upflow rate, the film model does a reasonable job of describing the feed region using the same value of 0.4 for τ_{av}/τ^* as at flooding. Therefore, the model can be used over a wider range of conditions than just flooding. The full implications of why $\tau_{av}/\tau^* = 0.4$ works best for all the runs are not yet known.

SUMMARY

The numerical studies presented here suggest that the condition of flooding takes place within the liquid film at the feed location. Flooding occurs when the interfacial shear is sufficiently high to cause a reversal in the direction of the velocity in the outer portion of the film. Application of this model shows good agreement with the axial profile of the mean film thickness as measured in the feed region. The shear stress is less than that computed from the measured pressure gradient assuming parallel nonaccelerating flows. The difference is attributed to the very large accelerations which take place for the gas flow around these large waves.

Acknowledgements—The financial support of the U.S. Office of Naval Research and the Shell Development Co. is gratefully acknowledged.

REFERENCES

Bankoff, S. G. & Lee, S. C. 1986 A critical review of the flooding literature. In *Multiphase Science and Technology*, Chap. 2 (Edited by Hewitt, G. F., Delhaye, J. M. & Zuber, N.), pp. 95–180. Hemisphere, New York.

Gosman, A. D. & Ideriah, F. J. K. 1976 Teach-T: a general computer program for two-dimensional, turbulent, recirculating flows. Dept of Mech. Engng, Imperial College, London.

Govan, A. H., Hewitt, G. F., Richter, H. J. & Scott, A. 1991 Flooding and churn flow in vertical pipes. *Int. J. Multiphase Flow* **17**, 27–44.

HUANG, P. G., LAUNDER, B. E. & LESCHZINER, M. A. 1985 Discretization of nonlinear convection processes: a broad-range comparison of four schemes. *Comput. Meth. Appl. Mech. Engng* **48,** 1–24.

LACY, C. E. 1992 Flooding and wavy films in vertical annular gas–liquid flows. Ph. D. Dissertation, Univ. of Houston, Houston, TX.

LACY, C. E. & DUKLER, A. E. 1994 Flooding in vertical tubes—I. Experimental studies of the entry region. *Int. J. Multiphase Flow* **20,** 219–233.

LEONARD, B. P. 1979 A stable and accurate convective modelling procedure based on quadratic upstream interpolation. *Comput. Meth. Appl. Mech. Engng* **19,** 59–98.

LOPES, J. C. B. & DUKLER, A. E. 1986 Droplet entrainment in vertical annular flow and its contribution to momentum transfer. *AIChE Jl* **32,** 1500–1515.

PATANKAR, S. V. 1980 *Numerical Heat Transfer and Fluid Flow*. Hemisphere, New York.

POLLARD, A. & SIU, A. L.-W. 1982 The calculation of some laminar flows using various discretisation schemes. *Comput. Meth. Appl. Mech. Engng* **35,** 293–313.

RYSKIN, G. & LEAL, L. G. 1983 Orthogonal mapping. *J. Comput. Phys.* **50,** 71–100.

ZABARAS, G. J. & DUKLER, A. E. 1988 Countercurrent gas–liquid annular flow, including the flooding state. *AIChE Jl* **34,** 389–396.

APPENDIX

Navier–Stokes Equations

To obtain [5] and [6] from [4], let $\mathbf{J} = (\rho \mathbf{V}\mathbf{V} + P\mathbf{I} - \tau)$. Then, $\nabla \cdot \mathbf{J} = \mathbf{B}$ becomes

$$\frac{1}{h_\xi h_\eta}\left[\frac{\partial}{\partial \xi}(h_\eta J_{\xi\xi}) + \frac{\partial}{\partial \eta}(h_\xi J_{\eta\xi}) + J_{\xi\eta}\frac{\partial h_\xi}{\partial \eta} - J_{\eta\eta}\frac{\partial h_\eta}{\partial \xi}\right] = B_\xi \tag{A1}$$

and

$$\frac{1}{h_\xi h_\eta}\left[\frac{\partial}{\partial \xi}(h_\eta J_{\xi\eta}) + \frac{\partial}{\partial \eta}(h_\xi J_{\eta\eta}) + J_{\eta\xi}\frac{\partial h_\eta}{\partial \xi} - J_{\xi\xi}\frac{\partial h_\xi}{\partial \eta}\right] = B_\eta \tag{A2}$$

for the ξ and η directions, respectively, and the $\mathbf{J}$ components are given as

$$J_{\xi\xi} = \rho u^2 + P - 2\mu\epsilon_{\xi\xi}, \tag{A3a}$$

$$J_{\xi\eta} = J_{\xi\eta} = \rho uv - 2\mu\epsilon_{\xi\eta} \tag{A3b}$$

and

$$J_{\eta\eta} = \rho v^2 + P - 2\mu\epsilon_{\eta\eta}. \tag{A3c}$$

Substituting [25] into [24] and multiplying through by $h_\xi h_\eta$ results in [5] and [6] in terms of the rates of strains, ϵ_{ij}. The values of ϵ_{ij} are defined as

$$\epsilon_{\xi\xi} = \frac{1}{h_\xi}\left(\frac{\partial u}{\partial \xi} + \frac{v}{h_\eta}\frac{\partial h_\xi}{\partial \eta}\right), \tag{A4a}$$

$$\epsilon_{\xi\eta} = \frac{1}{2}\left[\frac{1}{h_\xi}\frac{\partial v}{\partial \xi} + \frac{1}{h_\eta}\frac{\partial u}{\partial \eta} - \frac{1}{h_\xi h_\eta}\left(u\frac{\partial h_\xi}{\partial \eta} + v\frac{\partial h_\eta}{\partial \xi}\right)\right] \tag{A4b}$$

and

$$\epsilon_{\eta\eta} = \frac{1}{h_\eta}\left(\frac{\partial v}{\partial \eta} + \frac{u}{h_\xi}\frac{\partial h_\eta}{\partial \xi}\right). \tag{A4c}$$

The body force, $\mathbf{B}$, in the (x, y) coordinate system is given by

$$\mathbf{B} = -\rho g \mathbf{j}, \tag{A5}$$

where $\mathbf{j}$ is the unit vector in the y direction. In the (ξ, η) domain, this corresponds to

$$B_\xi = -\rho g \mathbf{j} \cdot \mathbf{e}_1 = -\rho g \mathbf{j} \cdot \left(\frac{1 \partial x}{h_\xi \partial \xi}\mathbf{i} + \frac{1}{h_\xi}\frac{\partial y}{\partial \xi}\mathbf{j}\right) = -\frac{\rho g}{h_\xi}\frac{\partial y}{\partial \xi} \tag{A6}$$

and

$$B_\eta = -\rho g \mathbf{j} \cdot \mathbf{e}_2 = -\rho g \mathbf{j} \cdot \left(\frac{1}{h_\eta} \frac{\partial x}{\partial \eta} \mathbf{i} + \frac{1}{h_\eta} \frac{\partial y}{\partial \eta} \mathbf{j} \right) = -\frac{\rho g}{h_\eta} \frac{\partial y}{\partial \eta}, \qquad \text{[A7]}$$

where $\mathbf{e}_1$ and $\mathbf{e}_2$ are the unit vectors in the (ξ, η) domain; for further details, see Lacy (1992). Substituting [A4], [A6] and [A7] into [5] and [6] yields

$$\begin{aligned} &\frac{\partial}{\partial \xi} (h_\eta \rho u^2) + \frac{\partial}{\partial \eta} [h_\xi \rho u v) + \rho u v \frac{\partial h_\xi}{\partial \eta} - \rho v^2 \frac{\partial h_\eta}{\partial \xi} \\ &\quad = -h_\eta \rho g \frac{\partial y}{\partial \xi} - h_\eta \frac{\partial P}{\partial \xi} + \frac{\partial}{\partial \xi} \left(\frac{\mu h_\eta}{h_\xi} \frac{\partial u}{\partial \xi} \right) + \frac{\partial}{\partial \eta} \left(\frac{\mu h_\xi}{h_\eta} \frac{\partial u}{\partial \eta} \right) + \frac{\partial}{\partial \xi} \left[\frac{\mu h_\eta}{h_\xi} \left(\frac{\partial u}{\partial \xi} + \frac{2v}{h_\eta} \frac{\partial h_\xi}{\partial \eta} \right) \right] \\ &\quad\quad - \frac{2\mu}{h_\eta} \frac{\partial h_\eta}{\partial \xi} \left(\frac{\partial v}{\partial \eta} + \frac{u}{h_\xi} \frac{\partial h_\eta}{\partial \xi} \right) + \frac{\partial}{\partial \eta} \left[\mu \left(\frac{\partial v}{\partial \xi} - \frac{u}{h_\eta} \frac{\partial h_\xi}{\partial \eta} - \frac{v}{h_\eta} \frac{\partial h_\eta}{\partial \xi} \right) \right] \\ &\quad\quad + \mu \frac{\partial h_\xi}{\partial \eta} \left[\frac{1}{h_\xi} \frac{\partial v}{\partial \xi} + \frac{1}{h_\eta} \frac{\partial u}{\partial \eta} - \frac{1}{h_\xi h_\eta} \left(u \frac{\partial h_\xi}{\partial \eta} + v \frac{\partial h_\eta}{\partial \xi} \right) \right] \end{aligned} \qquad \text{[A8]}$$

and

$$\begin{aligned} &\frac{\partial}{\partial \xi} (h_\eta \rho u v) + \frac{\partial}{\partial \eta} (h_\xi \rho v^2) + \rho u v \frac{\partial h_\eta}{\partial \xi} - \rho u^2 \frac{\partial h_\xi}{\partial \eta} \\ &\quad = -h_\xi \rho g \frac{\partial y}{\partial \eta} - h_\xi \frac{\partial P}{\partial \eta} + \frac{\partial}{\partial \xi} \left(\frac{\mu h_\eta}{h_\xi} \frac{\partial v}{\partial \xi} \right) + \frac{\partial}{\partial \eta} \left(\frac{\mu h_\xi}{h_\eta} \frac{\partial v}{\partial \eta} \right) + \frac{\partial}{\partial \eta} \left[\frac{\mu h_\xi}{h_\eta} \left(\frac{\partial v}{\partial \eta} + \frac{2u}{h_\xi} \frac{\partial h_\eta}{\partial \xi} \right) \right] \\ &\quad\quad - \frac{2\mu}{h_\xi} \frac{\partial h_\xi}{\partial \eta} \left(\frac{\partial u}{\partial \xi} + \frac{v}{h_\eta} \frac{\partial h_\xi}{\partial \eta} \right) + \frac{\partial}{\partial \xi} \left[\mu \left(\frac{\partial u}{\partial \eta} - \frac{u}{h_\xi} \frac{\partial h_\xi}{\partial \eta} - \frac{v}{h_\xi} \frac{\partial h_\eta}{\partial \xi} \right) \right] \\ &\quad\quad + \mu \frac{\partial h_\eta}{\partial \xi} \left[\frac{1}{h_\xi} \frac{\partial v}{\partial \xi} + \frac{1}{h_\eta} \frac{\partial u}{\partial \eta} - \frac{1}{h_\xi h_\eta} \left(u \frac{\partial h_\xi}{\partial \eta} + v \frac{\partial h_\eta}{\partial \xi} \right) \right] \end{aligned} \qquad \text{[A9]}$$

for ξ and η, respectively.

Boundary Conditions for Mapping at $\xi = 1$

To compute the value of $\delta^{n-1}(\eta_i)$ requires the orthogonality relationship of

$$\frac{\partial x}{\partial \xi} \frac{\partial x}{\partial \eta} + \frac{\partial y}{\partial \xi} \frac{\partial y}{\partial \eta} = 0, \qquad \text{[A10]}$$

which is equivalent to [14]. Rewriting this equation and [2] for the nth iteration yields

$$\frac{\partial y^n}{\partial \xi} = -\left[\frac{\dfrac{\partial x^n}{\partial \eta}}{\dfrac{\partial y^n}{\partial \eta}} \right] \frac{\partial x^n}{\partial \xi} = -a^n \frac{\partial x^n}{\partial \xi} \qquad \text{[A11]}$$

and

$$(h_\xi^n)^2 = \left(\frac{\partial x^n}{\partial \xi} \right)^2 + \left(\frac{\partial y^n}{\partial \xi} \right)^2. \qquad \text{[A12]}$$

Though the values of x and y are to be calculated for the nth iteration, the value of a^n is unknown, but can be approximated by using a^{n-1}. By substituting [A11] into [A12] with $a^n = a^{n-1}$, an equation for $\partial x^n / \partial \xi$ can be obtained as

$$\frac{\partial x^n}{\partial \xi} = \sqrt{\frac{(h_\xi^n)^2}{1 + (a^{n-1})^2}} \qquad \text{[A13]}$$

and

$$\frac{\partial y^n}{\partial \xi} = -a^{n-1} \sqrt{\frac{(h_\xi^n)^2}{1 + (a^{n-1})^2}}. \qquad \text{[A14]}$$

This completes the specification of the boundary conditions needed to solve [11] and [12] for each iteration to change $h_\xi(1, \eta)$.

Algorithm for $\delta^{n-1}(\eta_i)$

The choice of $\delta^{n-1}(\eta_i)$ used in [15] is given by

$$\delta^{n-1}(\eta_i) = \frac{a}{\Delta P_{\mathrm{Max}}^{n-1}} \{\Delta P^{n-1}(1, \eta_i) - b[\Delta P^{n-1}(1, \eta_{i+1}) - \Delta P^{n-1}(1, \eta_i)]\}, \qquad \text{[A15]}$$

where ΔP is the difference between the specified pressure and P_{G} calculated from [10], $\Delta P_{\mathrm{Max}}^{n-1}$ signifies the maximum computed pressure difference along the interface during the $(n-1)$th iteration, $a = 2 \times 10^{-6}$ m for $\Delta P_{\mathrm{Max}}^{n-1} > 5\ \mathrm{N/m^3}$ and 3×10^{-7} m for $\Delta P_{\mathrm{Max}}^{n-1} < 5\ \mathrm{N/m^3}$, $b = 4$ and the subscript $i + 1$ refers to the neighboring numerical grid node located vertically immediately above node i. The values of a and b were chosen by a trial-and-error process to obtain a quick, but stable solution. The larger value of a was used to obtain the approximate solution, and the smaller was used to obtain the final solution.